Materials Reports Solidwaste & Ecomaterials

Materials Reports: Solidwaste and Ecomaterials

Journal Homepage: www.sciopen.com/journal/3078-4093

Original Research Report

Dimensional engineering of fly ash-grown carbon nanomaterials for sustainable cement reinforcement

Yin Yang, Henglong Ren, Xinlong Ma *

State Key Laboratory of Heavy Oil Processing, China University of Petroleum, Beijing 102249, China

Abstract: Global solid waste management and construction material sustainability converge in fly ash (FA), with approximately 1700 million tons generated annually, while current utilization fails to adequately address its environmental burdens. This work establishes an ecomaterials paradigm by synthesizing controllable-sized carbon nanomaterials in situ on FA, converting FA into high-performance cement reinforcement materials. Through chemical vapor deposition, planar graphene is grown via intrinsic oxide catalysis and tubular carbon nanotubes on iron-functionalized FA, creating catalyst-integrated composites that eliminate purification steps and dispersion challenges. The substrate-bonded nanomaterials drastically reduce production costs compared to commercial alternatives while ensuring optimal distribution in cementitious systems. These solid waste-derived ecomaterials function as multifunctional additives at dosages of 5%–20%, reducing dependence on virgin cement while delivering complementary performance enhancements: graphene provides exceptional early-age enhancement (+36.96% flexural strength at 3 d in mortar, +18.55% compressive strength at 7 d in concrete), whereas carbon nanotubes provide sustained reinforcement maintaining advantages through 28 d across both mortar and concrete systems. This catalyst-integrated approach simultaneously addresses solid waste accumulation, reduces cement-related emissions, and delivers superior material performance compared to conventional alternatives, demonstrating a scalable pathway for solid waste valorization through dimensional engineering of carbon nanomaterials.

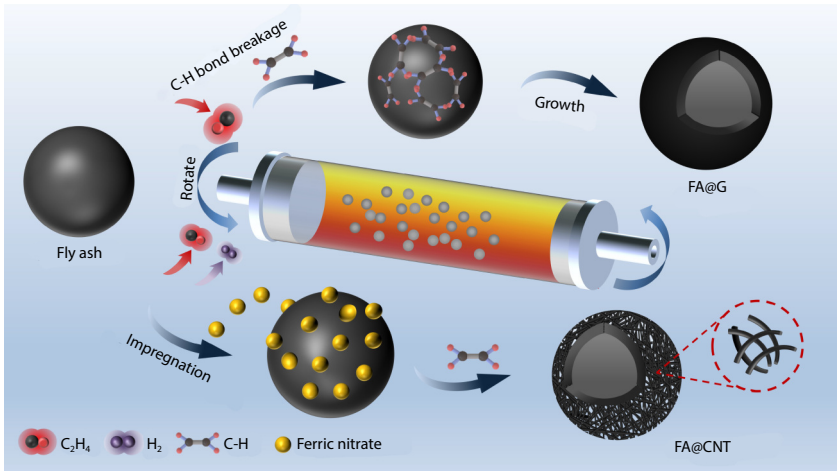

Keywords: fly ash, graphene, carbon nanotubes, chemical vapor deposition, solid waste valorization

Citation: Y. Yang, H. Ren, X. Ma. Dimensional engineering of fly ash-grown carbon nanomaterials for sustainable cement reinforcement. *Materials Reports: Solidwaste and Ecomaterials*, 2025, 1: 9520021. https://doi.org/10.26599/MRSE.2025.9520021.

1. Introduction

The construction industry consumes over 4.4 billion tons of cement annually, contributing approximately 8% of global anthropogenic CO_2 emissions while depleting non-renewable limestone resources[1-5]. Concurrently, coal-based power generation produces 1.7 billion tons of fly ash (FA) per year, with over 60% accumulating in landfills and posing groundwater contamination risks[6-9]. The convergence of these challenges necessitates transformative materials strategies that simultaneously address resource depletion, emission reduction, and solid waste valorization.

*Correspondence to X. Ma, maxl@cup.edu.cn

Received 14 October 2025; Received in revised form 26 November 2025; Accepted 5 December 2025

Current approaches to mitigating these interconnected problems remain constrained by fundamental technical and economic limitations. Conventional approaches incorporate FA at 15%–30% dosages as a supplementary cementitious material[10,11], yet fail to elevate this waste beyond low-value applications or substantially enhance long-term performance. More advanced strategies have explored carbon nanomaterial reinforcement in cementitious systems, leveraging their superior tensile strength, high aspect ratios, and multiple nanoscale enhancement mechanisms, including pore filling, heterogeneous nucleation, and crack-bridging[12-15]. However, hydrophobic surfaces and strong van der Waals interactions cause agglomeration in aqueous cement, preventing uniform distribution even at minimal loadings[16,17]. Surfactant-based dispersion strategies further escalate costs and compromise nanomaterial properties, rendering this approach economically unviable for large-scale construction.

A critical insight emerges from the chemical composition of FA itself. This industrial waste contains metal oxides—particularly SiO_2, Al_2O_3, and Fe_2O_3—that are known to catalyze carbon nanomaterial formation under appropriate thermal conditions[18]. For graphene synthesis, surface oxygen functionalities on these intrinsic oxides can serve as active sites that lower energy barriers for carbon ring nucleation, enabling spontaneous growth without supplementary catalysts[19]. Carbon nanotube formation, conversely, requires transition metal catalysts such as iron or nickel, which can be readily introduced onto FA surfaces through simple impregnation methods[20,21]. This catalytic functionality positions FA as an ideal substrate for in situ carbon nanomaterial synthesis.

Chemical vapor deposition (CVD) enables exploitation of this catalytic potential[22]. The in-situ growth ensures uniform nanomaterial distribution across FA surfaces, with each particle serving simultaneously as a catalyst support and dispersion matrix. By maintaining this substrate-anchored configuration throughout cement application, the approach circumvents purification and dispersion barriers, reframing FA from waste into a multifunctional ecomaterial platform.

An important question concerns how nanomaterial dimensionality influences reinforcement performance. Graphene's two-dimensional (2D) planar structure provides high surface area favoring hydration acceleration and pore refinement[23], while the one-dimensional (1D) tubular architecture of carbon nanotube (CNT) offers high aspect ratios conducive to crack-bridging and sustained load transfer[24]. While both nanomaterial types have been explored in cementitious systems, comparative studies systematically evaluating their respective performance advantages remain limited. Liu et al.[25] and Yao et al.[26] found CNTs superior to graphene sheets in fracture toughness at 0.05 wt%, attributing this to better crack bridging, while other work suggests graphene's planar geometry provides advantages in pore refinement and early-age strength development[27,28]. However, these studies compare commercial nanomaterials at single or differing concentrations, with performance potentially confounded by variable dispersion quality, surfactant chemistry, and nanomaterial purity—factors known to critically influence cement composite behavior.

This work demonstrates that controlled dimensional engineering of carbon nanomaterials on FA substrates provides a scalable approach to solid waste valorization. Through systematic synthesis and performance evaluation, the study reveals dimension-selective reinforcement characteristics: graphene-functionalized FA enhances early-age cement properties, while CNT-decorated particles improve long-term performance. By converting disposal-bound industrial waste into tailored, high-performance ecomaterials, this substrate-integrated strategy provides a practical pathway toward implementing a circular economy in construction materials.

2. Experimental section

2.1. Synthesis of FA@G composites

FA@G composites were synthesized using CVD in a rotary tube furnace. Raw FA was loaded into the reaction tube, and the system was purged with Ar (0.4 L min^{-1}) to remove air. The furnace was heated to the target reaction temperature at 10 °C min^{-1} under atmospheric pressure. Upon reaching the set temperature, the tube rotation was activated (40 rpm), and ethylene (C_2H_4, 0.4 L min^{-1}) was introduced as the carbon source, maintaining an Ar:C_2H_4 molar ratio of 1:1. After the designated reaction time, C_2H_4 flow and tube rotation were stopped, and the system was cooled to room temperature under Ar atmosphere (0.4 L min^{-1}) to obtain FA@G composites.

To investigate the effects of processing conditions on FA@G growth and properties, the reaction temperature was fixed at 720 °C, while reaction times were varied at 8, 12, and 16 min, with the resulting composites designated as FA@G-8, FA@G-12, and FA@G-16, respectively. Gas flow rates were maintained constant throughout all experiments.

2.2. Synthesis of FA@CNT composites

An iron catalyst was first deposited onto FA surfaces through wet impregnation. $Fe(NO_3)_3{\cdot}9H_2O$ (5 wt% relative to FA) was dissolved in anhydrous ethanol with 15 min of ultrasonication. FA powder was then added to the solution and impregnated for 30 min under stirring. The mixture was dried at 40 °C for 8 h and subsequently calcined in a muffle furnace at 800 °C for 2 h under an air atmosphere to produce the Fe-functionalized FA catalyst.

CVD synthesis of FA@CNT was performed in a rotary tube furnace. The prepared catalyst (10 g) was finely ground and loaded into the reaction tube. After purging with Ar (0.4 L min^{-1}), the furnace was heated to the reaction temperature at 10 °C min^{-1}. Upon reaching the set temperature, tube rotation was activated (40 rpm), and H_2 gas (0.1 L min^{-1}) was introduced for 10 min to reduce the iron catalyst. Subsequently, C_2H_4 (0.4 L min^{-1}) was introduced while maintaining the Ar flow, achieving an Ar:C_2H_4 molar ratio of 1:1. After the designated reaction time, C_2H_4 flow and rotation were stopped, and the system was cooled to room temperature under an Ar atmosphere to obtain FA@CNT composites.

To investigate the effects of processing conditions on FA@CNT growth and properties, the reaction temperature

was fixed at 700 °C, while reaction times were varied at 45, 60, and 75 min, with the resulting composites designated as FA@CNT-45, FA@CNT-60, and FA@CNT-75, respectively.

2.3. Preparation of cement-based materials

2.3.1. Cement mortar specimens

To evaluate the influence of composite dosage on the mechanical properties of cement mortar, specimens were prepared according to the mix proportions shown in Table 1. Six experimental groups were designed with composite replacement levels of 0% (control), 5%, 10%, 20%, 30%, and 40% by mass of cement.

Materials were pre-weighed according to the formulations and mixed using a planetary mortar mixer following the sequence: (1) cement and composites (or FA for control) were dry-mixed at low speed (140 rpm) for 1 min; (2) standard sand was added and dry-mixed for 2 min; (3) water was gradually added over 30 s followed by high-speed mixing (285 rpm) for 2 min; (4) after a 30 s pause to scrape the bowl walls, final high-speed mixing was conducted for 1.5 min. The complete mixing procedure is illustrated in Fig. S1. The fresh mortar was cast into prismatic molds (40 mm×40 mm×160 mm) in two layers with vibration compaction after each layer. After casting, the surface was leveled with a straight edge. Specimens were demolded after 24 h and cured in a standard curing room at (20±2) °C and >95% relative humidity for 3, 7, and 28 d prior to testing.

2.3.2. Cement concrete specimens

To investigate composite effects on the mechanical properties of concrete, specimens were prepared according to the mix proportions shown in Table 2. Five experimental groups were designed where composites replaced FA at levels of 0% (control), 5%, 10%, 20%, and 30% by mass. Each group consisted of six replicate specimens.

Materials were pre-weighed, thoroughly mixed, and cast into cubic molds (150 mm×150 mm×150 mm). After demolding, specimens were cured under standard conditions ((20±2) °C, >95% relative humidity) for 7 d and 28 d prior to testing.

2.4. Material characterization

Morphology and microstructure of FA@G and FA@CNT composites were characterized by scanning electron microscopy (SEM, Quanta 200F, FEI). Raman spectroscopy was performed on a spectrometer (Horiba Jobin Yvon LabRAM HR800) with 633 nm He-Ne laser excitation. X-ray diffraction (XRD) patterns were collected on a Bruker D8 Advance diffractometer. Thermogravimetric analysis (TGA) was conducted on a Shimadzu thermogravimetric analyzer under an oxygen atmosphere with a heating rate of 10 °C min^{-1} to determine thermal stability and carbon content.

2.5. Mechanical property testing

Cement mortar: Flexural and compressive strength tests were performed according to standard procedures. Flexural testing was conducted at a loading rate of 100 N s^{-1}, and compressive testing of the fractured halves was performed at 2.4 kN s^{-1}. Results represent the average of three specimens per group.

Cement concrete: Compressive strength testing was performed using a 2000 kN universal testing machine. Specimens were centered between the compression platens and loaded at 0.5–0.8 MPa s^{-1} until failure. Results represent the average of three specimens per group.

3. Results and discussion

3.1. Characterization of FA@G composites

FA from coal-fired power plants contains various metal oxides, including SiO_2, Al_2O_3, and Fe_2O_3[29,30]. Density functional theory calculations have shown that surface oxygen atoms on these oxides can catalyze hydrocarbon decomposition and carbon nucleation[31]. During CVD, the carbon source C_2H_4 undergoes pyrolysis on oxide surfaces at elevated temperatures, breaking C–H bonds and forming dispersed carbon hexagonal rings, with oxygen atoms serving as nucleation sites. These hexagonal units progressively connect to form graphene layers on the oxide surface.

SEM images (Fig. 1a–c) showed the morphological changes of FA before and after graphene coating. Pristine FA

Table 1. Mix proportions for cement mortar specimens.

Sample	Cement (g)	Water (mL)	Composites (g)	Granule (g)
P.O 42.5	450	225	0	1350
FA@G-1/FA@CNT-1	427.5	225	22.5	1350
FA@G-2/FA@CNT-2	405	225	45	1350
FA@G-3/FA@CNT-3	360	225	90	1350
FA@G-4/FA@CNT-4	315	225	135	1350
FA@G-5/FA@CNT-5	270	225	180	1350

Table 2. Mix proportions for cement concrete specimens.

Sample	Cement (g)	Aggregate (g)	Water (mL)	FA (g)	Composites (g)
CP	5.10	45.51	3.08	2.19	0
FA@G-5%/FA@CNT-5%	5.10	45.51	3.08	2.08	0.11
FA@G-10%/FA@CNT-10%	5.10	45.51	3.08	1.97	0.22
FA@G-20%/FA@CNT-20%	5.10	45.51	3.08	1.75	0.44
FA@G-30%/FA@CNT-30%	5.10	45.51	3.08	1.53	0.66

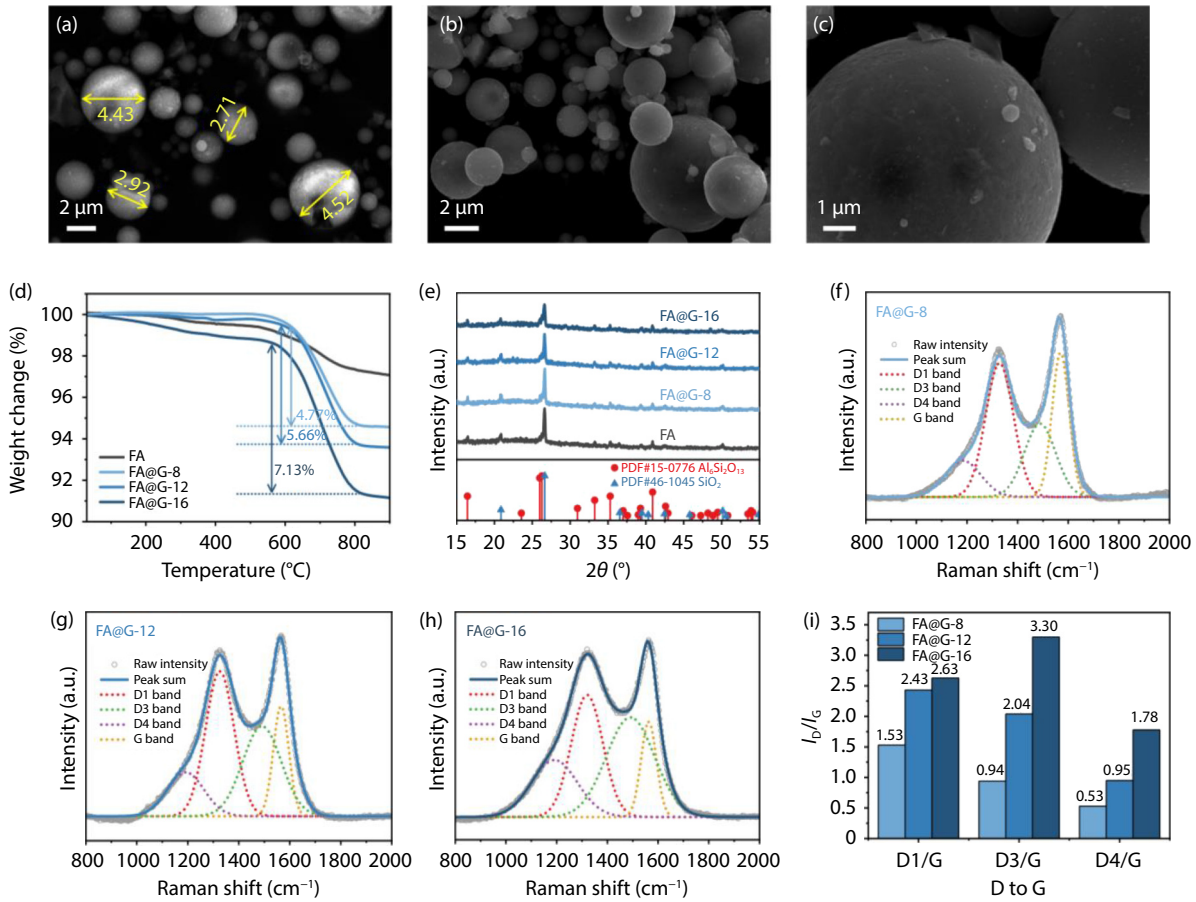

Fig. 1. Characterization of FA@G composites. (a) SEM image of pristine FA. (b, c) SEM images of FA@G-8. (d) TGA curves. (e) XRD patterns. (f–h) Raman spectra of FA@G-8, FA@G-12, and FA@G-16. (i) I_D/I_G ratios.

consisted of spherical particles ranging from 1 to 5 μm with smooth surfaces, and bright spots in the images indicated poor electrical conductivity. After CVD treatment, FA@G composites retained their spherical morphology, but the bright spots disappeared, indicating improved conductivity. Characteristic wrinkled features appeared on particle surfaces (Fig. 1c), confirming graphene layer formation.

TGA analysis (Fig. 1d) revealed that all FA@G composites began oxidative weight loss at approximately 500–600 °C in air. Carbon content increased with longer CVD reaction times, with FA@G-16 achieving the highest carbon loading. XRD patterns (Fig. 1e) showed that FA consisted primarily of mullite ($Al_6Si_2O_{13}$) and SiO_2 phases. After graphene coating, these characteristic peaks remained visible but with reduced intensity, indicating that the carbon layer did not alter the crystalline structure of the FA substrate. No graphitic carbon peaks appeared in FA@G samples, attributable to the thin carbon layer and low overall carbon content.

Raman spectroscopy (Fig. 1f–i) was used to evaluate carbon layer quality. The G band at ~1575 cm^{-1} corresponds to sp^2 hybridized carbon, while the D band indicates structural defects[32]. The D band was deconvoluted into three peaks[33]: D1 (~1325 cm^{-1}) representing disordered graphitic structures, D3 (~1489 cm^{-1}) attributed to amorphous carbon, and D4 (~1190 cm^{-1}) associated with sp^2-sp^3 bonding or C=C structures. The I_D/I_G ratio quantifies graphene quality, with lower values indicating better graphitization and fewer defects[34]. As shown in Fig. 1i, FA@G-8 exhibited the lowest I_D/I_G ratio, while this ratio increased for FA@G-12 and FA@G-16. This trend reflects a shift in growth mechanism: initially, oxide-catalyzed deposition produces relatively ordered carbon layers, but as thickness increases, thermal decomposition away from the catalytic surface dominates, depositing more disordered carbon[35]. These results establish FA@G-8 as the optimal synthesis condition, balancing carbon loading with structural quality, and this composite was subsequently selected for cement mortar performance evaluation.

3.2. Characterization of FA@CNT composites

SEM analysis (Fig. 2a–c) revealed that FA particle surfaces were covered by networks of carbon nanomaterials with mixed morphologies. The dominant structures were carbon nanofibers with diameters of approximately 200 nm, accompanied by smaller-diameter CNTs interspersed within the networks (Fig. 2b). Metal catalyst particles observed at the tips of these tubular structures (Fig. 2c, red circles) are consistent with tip-growth mechanisms. This morphological heterogeneity—combining CNTs, carbon nanofibers, and some amorphous carbon—reflects the diversity of metal catalyst particle sizes and catalytic activities distributed across FA surfaces.

TGA analysis (Fig. 2d) showed carbon content increased progressively with reaction time, reaching 30.44% for FA@CNT-75. The growth rate deceleration observed between

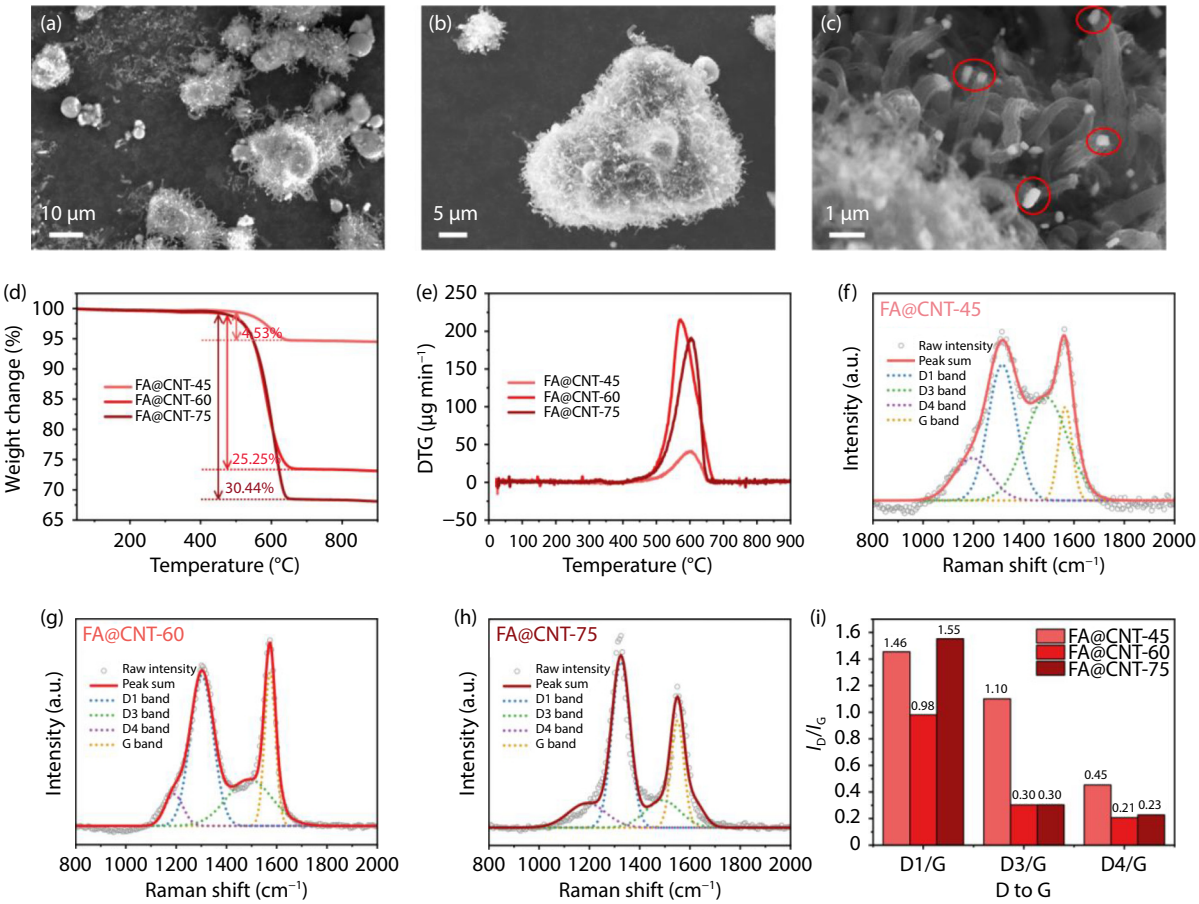

Fig. 2. Characterization of FA@CNT composites. (a–c) SEM images of FA@CNT. (d) TGA curves. (e) DTG curves. (f–h) Raman spectra of FA@CNT-45, FA@CNT-60, and FA@CNT-75. (i) I_D/I_G ratios.

60 and 75 min, where carbon content increased only 23% despite a 25% longer reaction time, suggests progressive catalyst deactivation. This behavior is characteristic of metal-catalyzed CNT synthesis, where catalyst particle encapsulation by disordered carbon progressively reduces active sites for tubular structure nucleation.

Derivative thermogravimetric analysis (DTG, Fig. 2e) showed that FA@CNT-60 exhibited a maximum oxidation temperature of 573 °C, lower than FA@CNT-45 (601 °C) and FA@CNT-75 (605 °C). Small-diameter CNTs oxidize at lower temperatures due to their high surface area and reactive edge sites, while larger-diameter carbon nanofibers require higher temperatures for complete oxidation. The lower DTG peak temperature of FA@CNT-60 suggests a higher proportion of smaller-diameter carbon structures in this sample[36].

Raman spectroscopy (Fig. 2f–i) provided detailed structural information through deconvolution of the D-band region into component peaks. The D1 band, representing graphitic lattice disorder, showed substantial variation: I_{D1}/I_G decreased from 1.46 (FA@CNT-45) to 0.98 (FA@CNT-60), then increased to 1.55 (FA@CNT-75), indicating that FA@CNT-60 achieves optimal crystallographic ordering. The D3 band, attributed to amorphous carbon, decreased from 1.10 (FA@CNT-45) to 0.30 (FA@CNT-60 and FA@CNT-75), suggesting that amorphous carbon content stabilizes after sufficient reaction time. Similarly, the D4 band, associated with sp^2-sp^3 bonding, decreased from 0.45 (FA@CNT-45) to approximately 0.21–0.23 (FA@CNT-60 and FA@CNT-75). The divergent behavior of D1 versus D3/D4 sub-bands indicates that the performance degradation in FA@CNT-75 primarily involves increased lattice disorder rather than accumulation of bulk amorphous carbon.

The multi-dimensional characterization establishes FA@CNT-60 as the optimal synthesis condition, exhibiting the lowest I_D/I_G ratio, minimal lattice disorder, and balanced carbon loading. This composite was subsequently selected for cement mortar performance evaluation.

3.3. Mechanical performance of FA@G-reinforced cement mortar

Based on the characterization results in Section 3.1, FA@G-8 exhibited optimal structural quality and was therefore selected for cement mortar performance evaluation. Mechanical testing evaluated FA@G-8 as a partial cement replacement in mortar formulations at dosages of 5%, 10%, 20%, 30%, and 40% (designated FA@G-1 through FA@G-5, corresponding to FA@G-8 composite replacing 5%–40% of cement mass), with compressive and flexural strength assessed at 3, 7, and 28 d of curing (Fig. 3). Each data point represents the average of three replicate specimens.

At 3 d, FA@G incorporation demonstrated significant strength improvements at low dosages (Fig. 3a and d). For compressive strength, FA@G-1 and FA@G-2 achieved 28.1

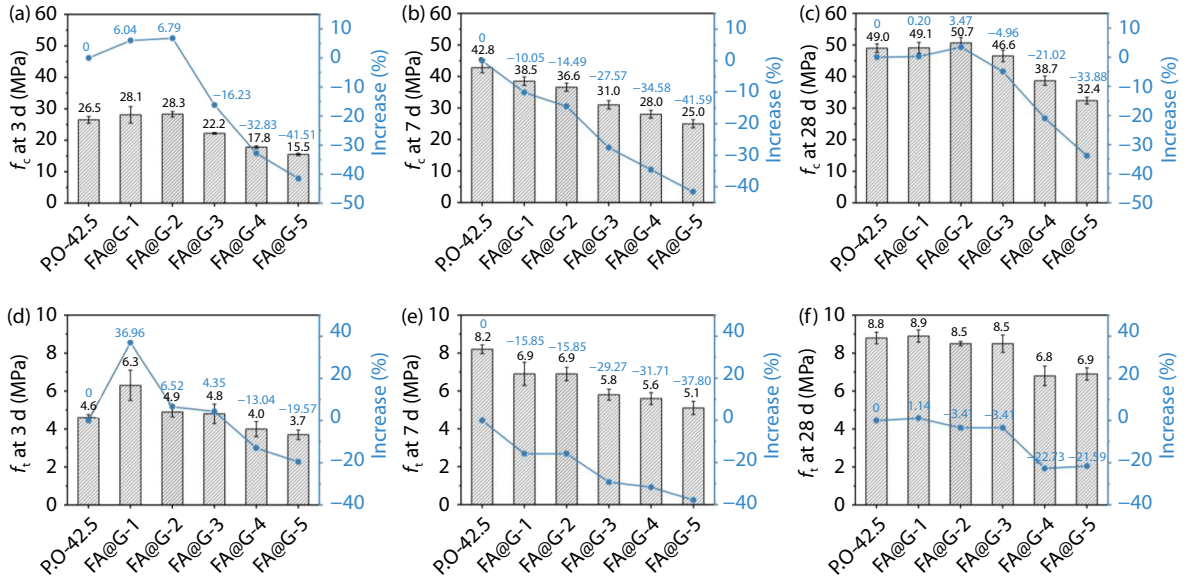

Fig. 3. Mechanical properties of FA@G-reinforced cement mortar. Compressive strength (f_c) at (a) 3 d, (b) 7 d, and (c) 28 d. Flexural strength (f_t) at (d) 3 d, (e) 7 d, and (f) 28 d.

MPa and 28.3 MPa, representing increases of 6.04% and 6.79% over the control (26.5 MPa), respectively. The enhancement was more pronounced for flexural strength, where FA@G-1 reached 6.3 MPa, a remarkable 36.96% improvement compared to the control (4.6 MPa), while FA@G-2 showed a 6.52% increase. The disproportionately large flexural enhancement relative to compressive gains suggests that graphene's planar structure is particularly effective at arresting mode I crack opening, which dominates flexural failure. The wrinkled graphene sheets, conformally coating FA particles, can bridge microcracks oriented perpendicular to tensile stress fields, providing crack deflection and closure forces that are less influential in the triaxial compression-dominated failure mode of compressive testing. However, higher replacement levels (≥20%, FA@G-3 to FA@G-5) resulted in progressive strength degradation, indicating that excessive FA@G adversely affects mechanical performance.

By 28 d, the enhancement effect persisted but diminished substantially in magnitude (Fig. 3c and f). FA@G-2 exhibited compressive strength of 50.7 MPa (3.47% increase over the 49.0 MPa control), while FA@G-1 showed minimal improvement (0.20%). For flexural strength, only FA@G-1 maintained a slight enhancement (1.14% over the 8.8 MPa control). Comparing across curing ages, the control gained 84.91% in compressive strength from 3 d to 28 d, while FA@G-1 gained only 74.73%, indicating that the control's continued hydration eventually narrows the performance gap. This temporal convergence suggests that graphene's reinforcement operates primarily during early curing stages rather than fundamentally altering the equilibrium microstructure. The exceptional early-age flexural enhancement likely reflects multiple synergistic mechanisms. Most significantly, graphene's planar structure provides efficient crack deflection and bridging under mode I loading, which dominates flexural failure. The disproportionately large flexural enhancement relative to compressive gains at 3 d strongly supports this crack-bridging mechanism, as the wrinkled graphene sheets conformally coating FA particles can bridge microcracks oriented perpendicular to tensile stress fields—effects that are less influential under the triaxial compression-dominated failure mode of compressive testing. Additionally, graphene's high-surface-area, oxygen-functionalized basal planes may promote early C-S-H formation through heterogeneous nucleation sites, while simultaneously providing physical densification of interfacial zones through nanoscale filling effects. The convergence of graphene-reinforced and control specimens by 28 d indicates that these advantages accelerate microstructural development rather than altering the final hydrated structure, as conventional extended curing eventually achieves comparable matrix density and crack resistance. These results establish 5% replacement (FA@G-1) as the optimal dosage, achieving consistent enhancement across all curing ages and testing modes, while 10% replacement (FA@G-2) performed comparably at early ages but offered limited long-term flexural benefit.

The performance decline at high dosages (>10%) reflects competing detrimental effects. Excessive FA reduces available clinker content below the threshold necessary to maintain adequate hydraulic reactivity, as the pozzolanic contribution of FA cannot fully compensate for lost alite and belite phases during early hydration[37]. Concurrently, increased graphene content may exceed the critical dispersion limit: despite substrate anchoring on FA particles, graphene sheets can still form local aggregates during mixing, particularly at interfaces between FA@G particles. These graphene-rich zones create weak planes with poor interfacial bonding to the cement matrix, acting as stress concentrators that initiate premature failure[38,39]. The relative immunity of flexural strength to moderate dosage increases (FA@G-2 and FA@G-3 show sustained enhancement at 3 d) compared to compressive strength suggests that graphene's crack-bridging benefits partially offset the matrix weakening effects under tensile

loading, but these advantages disappear under compressive stress states where aggregate interlock and matrix density become dominant[40].

3.4. Mechanical performance of FA@CNT-reinforced cement mortar

Based on the characterization results in Section 3.2, FA@CNT-60 exhibited optimal structural quality and was therefore selected for cement mortar performance evaluation. Mechanical testing evaluated FA@CNT-60 as a partial cement replacement at dosages of 5%, 10%, 20%, 30%, and 40% (designated FA@CNT-1 through FA@CNT-5), with compressive and flexural strength assessed at 3, 7, and 28 d (Fig. 4).

At 3 d, FA@CNT-1 achieved 31.1 MPa compressive strength, a remarkable 17.36% increase over the control (26.5 MPa), substantially exceeding the 6.04% improvement observed for FA@G-1 at equivalent dosage (Fig. 4a). This 2.9-fold enhancement advantage suggests that CNTs' one-dimensional, high-aspect-ratio morphology provides more effective early-age reinforcement than graphene's two-dimensional structure. The tubular geometry enables CNTs to span multiple cement grains, creating percolating mechanical networks even at low volume fractions, whereas graphene sheets primarily reinforce particle-scale interfacial regions. For flexural strength (Fig. 4d), FA@CNT-1, FA@CNT-2, and FA@CNT-3 reached 6.0 MPa, 5.8 MPa, and 5.5 MPa, representing increases of 30.43%, 26.09%, and 19.57% over the control (4.6 MPa), respectively. Notably, while FA@CNT-1's flexural enhancement (30.43%) approached FA@G-1's exceptional performance (36.96%), the broader effective dosage range (up to 20% for FA@CNT versus 10% for FA@G) indicates superior dispersion stability and a wider processing window for CNT-reinforced systems.

The critical distinction between CNT and graphene reinforcement emerged at 28 d (Fig. 4c and f). FA@CNT-1 maintained 4.29% compressive strength enhancement, retaining a significantly higher proportion of its early-age advantage (4.29% at 28 d from 17.36% at 3 d) compared to FA@G-1's retention of only approximately 3% (0.20% from 6.04%). More strikingly, for flexural strength, FA@CNT-2 exhibited 6.82% improvement at 28 d—its highest relative gain across all ages—while FA@G-1's flexural advantage collapsed from 36.96% at 3 d to 1.14% at 28 d. This temporal inversion, where CNT-reinforced mortars maintain or even improve their relative performance over time, fundamentally differs from the monotonic advantage decay observed in graphene systems. The sustained reinforcement reflects CNTs' superior crack-bridging capability, providing post-cracking toughness through mechanisms analogous to macro-fiber reinforcement. CNTs' flexible tubular structure enables them to accommodate interfacial deformations without debonding, maintaining load transfer capacity across evolving crack networks. In contrast, graphene's reinforcement operates primarily during early curing stages, with benefits diminishing as the control achieves comparable mechanical performance through continued hydration.

Comparing the two nanomaterial types reveals clear dimension-selective reinforcement characteristics aligned with their geometric complementarity. Graphene delivers exceptional early flexural enhancement through efficient mode I crack deflection by planar sheets, but loses this advantage by 28 d. CNT provides robust, sustained performance across all ages and stress states, with particular superiority in long-term flexural reinforcement. The optimal dosage ranges also diverge: FA@G exhibits a sharp optimum at 5% with rapid performance decline beyond 10%, whereas FA@CNT maintains benefits across 5%–10% with some flexural enhancement persisting to 20%. This broader tolerance likely reflects CNTs' superior resistance to re-agglomeration through mechanical entanglement, compared to graphene sheets' tendency to restack via π–π interactions[41,42]. The dimension-depen-

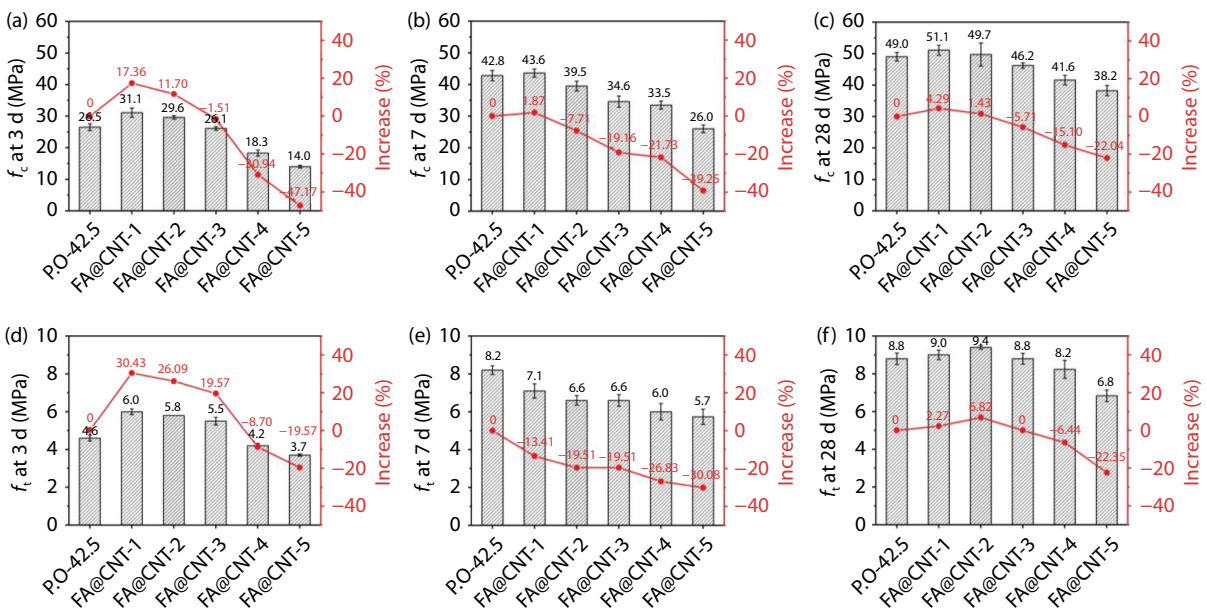

Fig. 4. Mechanical properties of FA@CNT-reinforced cement mortar. Compressive strength (f_c) at (a) 3 d, (b) 7 d, and (c) 28 d. Flexural strength (f_t) at (d) 3 d, (e) 7 d, and (f) 28 d.

dent mechanisms—graphene's early-age enhancement versus CNTs' mechanically-sustained reinforcement—establish that rational nanomaterial selection should prioritize application-specific performance requirements: graphene for rapid early strength development in precast applications, CNTs for sustained durability in long-service structures[30,43].

3.5. Mechanical performance in concrete applications

To validate the scalability of nanomaterial reinforcement from mortar to concrete systems, FA@G-8 and FA@CNT-60 composites were evaluated in concrete formulations containing coarse aggregates. The presence of coarse aggregates introduces additional interfacial zones and tortuosity, potentially altering optimal dosages and reinforcement mechanisms compared to mortar systems[44,45].

For FA@G-reinforced concrete (Fig. 5a and b), the early-age enhancement paralleled mortar behavior but with amplified magnitude. At 7 d, the 5% replacement (FA@G-5%) achieved 43.7 MPa, an 18.55% increase over the control, substantially exceeding the 6.04% improvement observed in mortar at the same age. This enhanced early performance in concrete is consistent with graphene's reported ability to refine interfacial transition zones around both fine and coarse aggregates, creating a more extensive network of strengthened interfacial regions compared to mortar's single aggregate size[46-48]. By 28 d, FA@G-5% maintained an 11.01% enhancement, outperforming the near-zero long-term advantage observed in mortar. The sustained benefit in concrete is consistent with previous observations of graphene's preferential accumulation at aggregate-paste interfaces[46-48], where crack deflection mechanisms may be more effective in the presence of coarse aggregates[49,50]. The optimal dosage remained 5% in concrete, consistent with mortar results, with higher replacements showing progressive performance decline attributable to the same agglomeration and clinker dilution mechanisms.

For FA@CNT-reinforced concrete (Fig. 5c and d), the performance profile differed markedly from both mortar and FA@G concrete. At 7 d, enhancements were modest, contrasting with the 17.36% improvement observed in mortar. However, at 28 d, FA@CNT-20% achieved 52.0 MPa, substantially exceeding both the control and all other dosages, including FA@CNT-5% and FA@CNT-10%. The 20% replacement level proved optimal in concrete, where the presence of coarse aggregates creates larger interfacial zones and longer crack paths that benefit from higher CNT concentrations to achieve effective reinforcement networks. Additionally, the vigorous mixing required for concrete workability may enhance CNT dispersion through aggregate-induced shear forces, mitigating agglomeration that limits dosage in mortar systems. The delayed enhancement, where 28-day performance far exceeds 7-day improvements, aligns with CNTs' crack-bridging mechanisms becoming increasingly important as the matrix densifies and develops shrinkage-induced microcracking[26,51]. The performance decline at 30% suggests that even

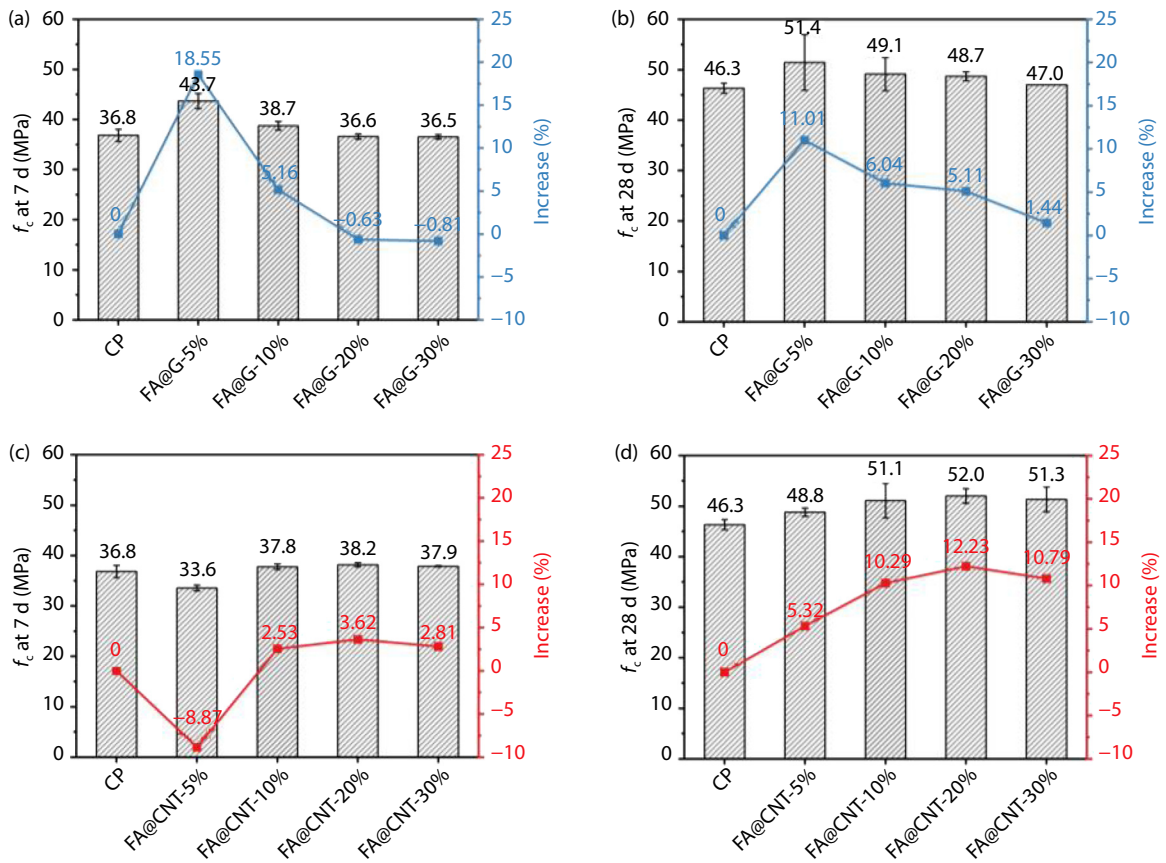

Fig. 5. Mechanical performance in concrete applications. Compressive strength of FA@G-reinforced concrete at (a) 7 d and (b) 28 d. Compressive strength of FA@CNT-reinforced concrete at (c) 7 d and (d) 28 d.

concrete's larger structural scale cannot accommodate unlimited CNT loading without encountering processing limitations or excessive FA dilution of the binder phase.

Comparing the two nanomaterials within the concrete system reveals dimension-selective reinforcement characteristics. FA@G demonstrated optimal performance at 5% replacement with maximum enhancement at early ages, while FA@CNT achieved optimal performance at 20% replacement with increasing relative advantages over time. These contrasting behaviors reflect their distinct geometric characteristics: graphene's planar structure efficiently refines interfacial zones at lower concentrations, whereas CNTs' tubular morphology requires higher loading to establish percolating networks across the three-dimensional concrete matrix. The temporal profiles further distinguish the two nanomaterials—graphene provides front-loaded kinetic enhancement while CNTs deliver sustained mechanical reinforcement—demonstrating that rational nanomaterial selection must consider both dimensional characteristics and application-specific performance requirements.

4. Conclusions

This study established dimension-selective reinforcement mechanisms for cementitious materials through in-situ growth of graphene and CNTs on fly ash substrates via CVD. The substrate-anchored nanomaterial architecture addresses long-standing dispersion challenges while enabling systematic investigation of geometry-dependent performance.

Comprehensive characterization identified optimal synthesis conditions: FA@G-8 exhibited minimal structural defects, while FA@CNT-60 achieved superior crystallographic ordering with balanced carbon loading. The distinct reaction durations and growth mechanisms—oxide-catalyzed surface deposition for graphene versus metal-catalyzed dissolution-precipitation for CNTs—produce structurally complementary nanomaterials anchored on the same FA substrate.

Mechanical testing revealed dimension-dependent reinforcement profiles across mortar and concrete systems. In cement mortar, FA@G delivered exceptional early-age flexural enhancement but diminished substantially by 28 d, consistent with early-stage reinforcement mechanisms including crack deflection and interfacial densification. FA@CNT provided sustained reinforcement, with FA@CNT-1 achieving a 30.43% flexural enhancement at 3 d and FA@CNT-2 maintaining a 6.82% enhancement at 28 d, demonstrating persistent crack-bridging effectiveness across dosage levels. In concrete applications, FA@G achieved optimal performance at 5% replacement with sustained early-age benefits, while FA@CNT demonstrated optimal performance at 20% replacement with maximum enhancement emerging at later ages.

These dimension-dependent behaviors establish rational selection criteria: graphene for rapid early strength in precast applications, CNTs for sustained durability in long-service structures. The scalable, substrate-anchored synthesis provides a practical pathway for deploying advanced nanomaterials in construction, simultaneously valorizing industrial waste streams and reducing cement consumption. The elimination of catalyst removal and dispersion processing steps—enabled by direct growth on fly ash substrates—positions this approach as economically viable for large-scale implementation.

Several research directions would further advance this dimensional engineering framework. Quantitative characterization of early-age hydration processes would provide direct validation of the acceleration mechanisms inferred from temporal strength evolution patterns. Detailed investigation of interfacial properties at the nanomaterial-cement matrix interface could elucidate the strengthening mechanisms observed in bulk mechanical performance, particularly for graphene-reinforced systems where exceptional early flexural enhancement was achieved. Long-term durability performance under aggressive environmental conditions—including freeze-thaw cycling, chemical attack, and carbonation—would complement the mechanical characterization conducted under standard curing and establish service-life predictions for practical applications. Investigation of synergistic effects in hybrid graphene-CNT systems represents a particularly promising direction, potentially combining graphene's early-age advantages with CNTs' sustained mechanical reinforcement to achieve optimized performance across multiple timescales. Finally, a comprehensive evaluation of the economic viability and environmental impact of this waste-valorization approach would quantify its benefits relative to conventional cement production and commercial nanomaterial incorporation, supporting the translation from laboratory demonstration to industrial implementation. These extensions would build upon the foundational dimensional engineering principles established herein, advancing rational design strategies for next-generation sustainable construction materials.

Author contribution statement

Yin Yang: Writing – original draft, Conceptualization, Data curation. **Henglong Ren:** Writing – review & editing, Visualization, Methodology, Conceptualization, Supervision. **Xinlong Ma:** Writing – review & editing, Conceptualization, Supervision, Project administration, Funding acquisition. All the authors have approved the final manuscript.

Declaration of competing interest

The authors declare that they have no known competing financial interests or personal relationships that could have appeared to influence the work reported in this paper.

Acknowledgements

This work is supported by the State Key Laboratory of Heavy Oil Processing, China University of Petroleum (No. SKL-HOP20250110).

Electronic Supplementary Material (ESM)

Supplementary material (schematic diagram illustrating the cement mortar mixing and specimen preparation procedure) is available in the online version of this article at https://doi.org/10.26599/MRSE.2025.9520021.

References

[1] Miao, C., Mu, S. Development and prospect of concrete technology in China. *Materials Reports: Solidwaste and Ecomaterials*, **2025**: 9520001. https://doi.org/10.26599/mrse.2025.9520001.

[2] Zhuang, S., Wang, X., Wang, D., et al. Soundness of steel slag as building materials: A review. *Materials Reports: Solidwaste and Ecomaterials*, **2025**: 9520004. https://doi.org/10.26599/mrse.2025.9520004.

[3] Haustein, K., Gerrard, M. B., Wentz, J. A. Heatwaves linked to emissions of individual fossil-fuel and cement producers. *Nature*, **2025**, 645(8080): 319–320. https://doi.org/10.1038/d41586-025-02596-6.

[4] Ma, J., Chen, Z., Yu, K., et al. Resource utilization of municipal solid waste incineration residues in cement-based materials: A review. *Materials Reports: Solidwaste and Ecomaterials*, **2025**: 9520007. https://doi.org/10.26599/mrse.2025.9520007.

[5] Zhu, K., Liang, Y., Yuan, J., et al. Flexible cement fibers with high toughness and water-activated setting behavior for construction. *Nature Communications*, **2025**, 16: 6529. https://doi.org/10.1038/s41467-025-61855-2.

[6] Alptekin, F. M., Zanoletti, A., Depero, L. E., et al. Accelerated carbonation of municipal waste fly ash for carbon sequestration: A review. *Environmental Chemistry Letters*, **2025**, 23(6): 1661–1687. https://doi.org/10.1007/s10311-025-01866-z.

[7] Darmansyah, D., You, S. J., Wang, Y. F. Advancements of coal fly ash and its prospective implications for sustainable materials in Southeast Asian countries: A review. *Renewable and Sustainable Energy Reviews*, **2023**, 188: 113895. https://doi.org/10.1016/j.rser.2023.113895.

[8] Li, Tong, Wang, Qinghe, Ren, Qingxin. Influence mechanism of steel slag aggregate/fly ash on mechanical properties and mass transport of engineered cementitious composite (ECC). *Materials Reports*, **2025**, 39(19): 153–159. (in Chinese)

[9] Zhao, T., Li, G., Zhang, S., et al. Enhancement effect of biochar on the immobilization of heavy metals and anions in MSWI fly ash/bottom ash–coal fly ash-based cementitious materials: Risk assessment model and mechanisms. *Journal of Hazardous Materials*, **2025**, 497: 139615. https://doi.org/10.1016/j.jhazmat.2025.139615.

[10] Song, J., Banthia, N., Yoo, D. Y. Effect of supplementary cementitious materials on durability of ultra-high-performance concrete: A review. *Cement and Concrete Composites*, **2025**, 163: 106198. https://doi.org/10.1016/j.cemconcomp.2025.106198.

[11] Gupta, S., Esmaeeli, H. S., Moini, R. Tough and ductile architected nacre-like cementitious composites. *Advanced Functional Materials*, **2024**, 34(39): 2313516. https://doi.org/10.1002/adfm.202313516.

[12] Park, J., Lee, Y., Hwang, H. Y., et al. Quantifying the concentration and dispersion of carbon nanotube in cement nanocomposites *via* confocal Raman microspectroscopy. *Carbon*, **2025**, 242: 120423. https://doi.org/10.1016/j.carbon.2025.120423.

[13] Chen, X., Park, J., Ji, W., et al. Unlocking the interaction mechanism of CNTs and C-S-H on enhancing elastic and viscoelastic properties of alite paste. *Advanced Science*, **2025**, 12(38): e05876. https://doi.org/10.1002/advs.202505876.

[14] Krystek, M., Ciesielski, A., Samorì, P. Graphene-based cementitious composites: Toward next-generation construction technologies. *Advanced Functional Materials*, **2021**, 31(27): 2101887. https://doi.org/10.1002/adfm.202101887.

[15] Lu, D., Ma, L. P., Zhong, J., et al. Growing nanocrystalline graphene on aggregates for conductive and strong smart cement composites. *ACS Nano*, **2023**, 17(4): 3587–3597. https://doi.org/10.1021/acsnano.2c10141.

[16] Liew, K. M., Kai, M. F., Zhang, L. W. Carbon nanotube reinforced cementitious composites: An overview. *Composites Part A: Applied Science and Manufacturing*, **2016**, 91: 301–323. https://doi.org/10.1016/j.compositesa.2016.10.020.

[17] Lee, S. Y., Nguyen, V. T., Chung, S. Y., et al. Hydration simulation of cement pastes reinforced with carbon nanotubes. *Construction and Building Materials*, **2023**, 384: 131333. https://doi.org/10.1016/j.conbuildmat.2023.131333.

[18] Hou, Y., Li, T., Lyu, Y., et al. The impact of fly ash and steel slag powder on sulfate erosion behavior of magnesium potassium phosphate cement paste. *Materials Reports*, **2025**, 39(18): 120–126. (in Chinese)

[19] Yang, S., Zhi, L., Tang, K., et al. Efficient synthesis of heteroatom (N or S)-doped graphene based on ultrathin graphene oxide-porous silica sheets for oxygen reduction reactions. *Advanced Functional Materials*, **2012**, 22(17): 3634–3640. https://doi.org/10.1002/adfm.201200186.

[20] Charlier, J. C., De Vita, A., Blase, X., et al. Microscopic growth mechanisms for carbon nanotubes. *Science*, **1997**, 275(5300): 646–649.

[21] Zhang, R., Zhang, Y., Wei, F. Horizontally aligned carbon nanotube arrays: Growth mechanism, controlled synthesis, characterization, properties and applications. *Chemical Society Reviews*, **2017**, 46(12): 3661–3715. https://doi.org/10.1039/C7CS00104E.

[22] Amontree, J., Yan, X., DiMarco, C. S., et al. Reproducible graphene synthesis by oxygen-free chemical vapour deposition. *Nature*, **2024**, 630(8017): 636–642. https://doi.org/10.1038/s41586-024-07454-5.

[23] Basquiroto de Souza, F., Yao, X., Gao, W., et al. Graphene opens pathways to a carbon-neutral cement industry. *Science Bulletin*, **2022**, 67(1): 5–8. https://doi.org/10.1016/j.scib.2021.08.018.

[24] Bai, Y., Yue, H., Wang, J., et al. Super-durable ultralong carbon nanotubes. *Science*, **2020**, 369(6507): 1104–1106. https://doi.org/10.1126/science.aay5220.

[25] Liu, B., Wang, J., Wei, Z., et al. Damping and microstructure of graphene/carbon nanotube-modified cement composites. *Buildings*, **2025**, 15(18): 3317. https://doi.org/10.3390/buildings15183317.

[26] Yao, Y., Lu, H. Mechanical properties and failure mechanism of carbon nanotube concrete at high temperatures. *Construction and Building Materials*, **2021**, 297: 123782. https://doi.org/10.1016/j.conbuildmat.2021.123782.

[27] Dalla, P. T., Tragazikis, I. K., Trakakis, G., et al. Multifunctional cement mortars enhanced with graphene nanoplatelets and carbon nanotubes. *Sensors*, **2021**, 21(3): 933. https://doi.org/10.3390/s21030933.

[28] Liu, J., Fu, J., Ni, T., et al. Fracture toughness improvement of multi-wall carbon nanotubes/graphene sheets reinforced cement paste. *Construction and Building Materials*, **2019**, 200: 530–538. https://doi.org/10.1016/j.conbuildmat.2018.12.141.

[29] Carneiro, G., Bier, T., Waida, S., et al. Treatment of Energy from Waste Plant fly-ash for blast furnace slag substitution as a Supplementary Cementitious Material. *Journal of Cleaner Production*, **2025**, 490: 144693. https://doi.org/10.1016/j.jclepro.2025.144693.

[30] Song, Y., Wang, X., Tu, S., et al. Effect of carbon nanotubes (CNTs) on the thermal deformation of cement-based materials. *Construction and Building Materials*, **2025**, 495: 143737. https://doi.org/10.1016/j.conbuildmat.2025.143737.

[31] Li, G., Li, N., Peng, S., et al. Highly efficient Nb_2C MXene cathode catalyst with uniform O-terminated surface for lithium–oxygen batteries. *Advanced Energy Materials*, **2021**, 11: 2002721. https://

doi.org/10.1002/aenm.202002721.
[32] Yang, Y., Du, H., Sun, D., et al. Boosting capacitive performance of S-doped carbon fibers *via* substrate-oriented activation methodology. *Industrial & Engineering Chemistry Research*, **2025**, 64(5): 2745–2757. https://doi.org/10.1021/acs.iecr.4c04038.
[33] Yang, Y., Du, H., Wang, A., et al. Excellent capacitive storage performance of *N*-doped porous carbon derived from the orientation-guidance coupled with *in situ* activation methodology. *Journal of Colloid and Interface Science*, **2024**, 673: 657–668. https://doi.org/10.1016/j.jcis.2024.05.237.
[34] Du, H., Yang, Y., Zhang, C., et al. Hierarchical porous carbon originated from the directing associated with activation as high-performance electrodes for supercapacitor and Li ion capacitor. *Journal of Power Sources*, **2024**, 614: 234988. https://doi.org/10.1016/j.jpowsour.2024.234988.
[35] Yang, Y., Song, H., Wang, J., et al. Frontier fabrication of silicon-based anodes: Synergistic enhancement of structural integrity and conductivity. *Chemical Engineering Journal*, **2025**, 506: 159918. https://doi.org/10.1016/j.cej.2025.159918.
[36] Martincic, M., Sandoval, S., Oró-Solé, J., et al. Thermal stability and purity of graphene and carbon nanotubes: Key parameters for their thermogravimetric analysis (TGA). *Nanomaterials*, **2024**, 14(21): 1754. https://doi.org/10.3390/nano14211754.
[37] Wang, P., Peng, Y., Ding, H., et al. Mechanical properties and microstructure characteristics of cementless ultra-high strength mortar activated by calcium carbide residue. *Materials Reports*, **2025**, 39(16): 124–132. (in Chinese)
[38] Dai, J., Wang, Y., Luo, L., et al. Effects of graphene oxide on hydration of cement-based materials at different curing temperatures. *Journal of Building Engineering*, **2025**, 111: 113268. https://doi.org/10.1016/j.jobe.2025.113268.
[39] Hu, Z. Y., Wan, Y., Duan, Y. J., et al. A review of the impact of graphene oxide on cement composites. *Nanomaterials*, **2025**, 15(3): 216. https://doi.org/10.3390/nano15030216.
[40] Gao, Y., Zou, F., Wang, S., et al. Redefining the cement substitution potential of recycled concrete powder using graphene oxide coating. *Cement and Concrete Composites*, **2025**, 164: 106276. https://doi.org/10.1016/j.cemconcomp.2025.106276.
[41] Shi, T., Li, Z., Guo, J., et al. Research progress on CNTs/CNFs-modified cement-based composites–A review. *Construction and Building Materials*, **2019**, 202: 290–307. https://doi.org/10.1016/j.conbuildmat.2019.01.024.
[42] Esnaashary, M. H., Karfarma, M., Rezaie, H. R., et al. The comparative study of gelatin/CNT-contained Mg-Ca-P bone cement with the plain and CNT-reinforced ones. *Journal of Bionic Engineering*, **2021**, 18(3): 623–636. https://doi.org/10.1007/s42235-021-0048-5.
[43] Hu, Z., Sun, X., Zhang, X., et al. Kinetic modulation of carbon nanotube growth in direct spinning for high-strength carbon nanotube fibers. *Journal of the American Chemical Society*, **2024**, 146(16): 11432–11439. https://doi.org/10.1021/jacs.4c01705.
[44] Hai, R., Cui, L., Zhai, S., et al. Research progress on compressive strength and durability of recycled concrete based on literature cluster analysis. *Materials Reports*, **2025**, 39(17): 50–58. (in Chinese)
[45] Wang, X., Shang, H., Lu, Z., et al. A review on the bonding performance of FRP bars to concrete: Mechanisms, testing methods, and influencing factors. *Materials Reports*, **2025**, 39(17): 265–272. (in Chinese)
[46] Sedaghat, A., Ram, M. K., Zayed, A., et al. Investigation of physical properties of graphene-cement composite for structural applications. *Open Journal of Composite Materials*, **2014**, 4(1): 12–21. https://doi.org/10.4236/ojcm.2014.41002.
[47] Sharma, M., Bishnoi, S. The interfacial transition zone: Microstructure, properties, and its modification. In: *Recent Advances in Structural Engineering, Volume 2*. Singapore: Springer Singapore, **2018**: 745–754. https://doi.org/10.1007/978-981-13-0365-4_63.
[48] Wang, Y., Gang, R., Peng, R., et al. Characterization of interfacial transition zone in compression-cast concrete. *Construction and Building Materials*, **2025**, 486: 141980. https://doi.org/10.1016/j.conbuildmat.2025.141980.
[49] Gholampour, A., Sofi, M., Alipooramirabad, H., et al. Performance of concrete containing pristine graphene-treated recycled concrete aggregates. *Resources, Conservation and Recycling*, **2023**, 199: 107266. https://doi.org/10.1016/j.resconrec.2023.107266.
[50] Dimov, D., Amit, I., Gorrie, O., et al. Ultrahigh performance nanoengineered graphene–concrete composites for multifunctional applications. *Advanced Functional Materials*, **2018**, 28(23): 1705183. https://doi.org/10.1002/adfm.201705183.
[51] Ahmad, J., Zhou, Z. Properties of concrete with addition carbon nanotubes: A review. *Construction and Building Materials*, **2023**, 393: 132066. https://doi.org/10.1016/j.conbuildmat.2023.132066.

Yin Yang is currently a PhD candidate at China University of Petroleum, Beijing, where her research focuses on the valorization of petroleum heavy components into advanced carbon nanomaterials. Her doctoral work centers on developing sustainable synthesis strategies that convert industrial waste streams into high-performance functional materials for construction and energy applications. Her research interests encompass chemical vapor deposition techniques, carbon nanomaterial characterization, and the development of eco-friendly cement reinforcement systems.

Xinlong Ma is an Associate Professor at China University of Petroleum, Beijing. His research group specializes in the high-value conversion of petroleum heavy fractions and industrial solid waste into advanced carbon materials, with a particular emphasis on the dimensional engineering of graphene and carbon nanotubes for functional applications. Dr. Ma's work bridges fundamental materials chemistry with practical applications in waste valorization, aiming to establish circular economy approaches for petroleum refining residues and coal combustion by-products.